Digital volume correlation analyses of synchrotron tomographic images

Julien Réthoré, Nathalie Limodin, Jean-Yves Buffiere, François Hild, Wolfgang Ludwig, Stéphane Roux

Digital volume correlation analyses of synchrotron tomographic images

J. Réthoré[a], N. Limodin[b], J-Y. Buffière[b]

F. Hild[c], W. Ludwig[b], S. Roux[c]

September 17, 2011

(a): Laboratoire de Mécanique des Contacts et des Structures (LAMCOS),

INSA-Lyon / UMR CNRS 5259

20 av. Albert Einstein, F-69621 Villeurbanne, France

Email: julien.rethore@insa-lyon.fr

(b): Laboratoire Matériaux, Ingénierie et Sciences (MATEIS),

INSA-Lyon / UMR CNRS 5510

7, avenue Jean Capelle, F-69621 Villeurbanne, France

Email: {nathalie.limodin,jean-yves.buffiere}@insa-lyon.fr

(c): Laboratoire de Mécanique et Technologie (LMT-Cachan)

ENS de Cachan / CNRS-UMR 8535 / Université Paris 6 / PRES UniverSud Paris

61 Avenue du Président Wilson, F-94235 Cachan Cedex, France

Email: {francois.hild,stephane.roux}@lmt.ens-cachan.fr

Abstract

3D images of nodular graphite cast iron samples obtained with synchrotron tomography are analyzed by resorting to digital volume correlation. This technique uses the material microstructure to measure displacement fields within a sample submitted to mechanical loading. Compared to classical 2D digital image correlation, the reconstructed volumes used by DVC tend to increase the uncertainty in the correlation calculations, yet elastic strains of the order of 10^{-3} can be measured. Displacement

fields around the front of a fatigue crack have also been measured by an extended version of DVC, and are used to extract stress intensity factors (in modes I, II and III) along the crack front. The values are in good agreement with finite element calculations when the experimentally measured displacements prescribed on the sample boundaries are considered as input in the numerical simulations.

Keywords: Elastic properties, full-field measurements, measurement uncertainties, stress intensity factor, X ray tomography.

List of notations

a	constant
a_p	amplitude associated with mode I reference fields
b_p	amplitude associated with mode II reference fields
d_j	additional degrees of freedom (enriched kinematics)
E	Young's modulus
f	picture of the reference configuration
g	picture of the deformed configuration
$\mathcal{H}$	Heaviside step function
h_j	enrichment function
i	imaginary unit
j	index
K_I, K_{II}, K_{III}	mode I, II, and III stress intensity factors
ℓ	element size
n_e	finite element shape function
$\mathbf{n}_j$	component of kinematic basis
n_x, n_y, n_z	number of nodes in the x, y and z directions
$\mathcal{N}$	total set of nodes
$\mathcal{N}_{\text{cut}}$	set of nodes that hold additional degrees of freedom
p	index
r	radius
R	load ratio
$\mathbf{u}$	displacement vector
u_j	degree of freedom
$\mathbf{v}$	in-plane displacement
$\mathbf{x}$	coordinate in the reference configuration
$\mathbf{x}_j$	coordinate of node j in the reference configuration
w	out-of-plane displacement

α	power
$\bar{\epsilon}$, $\tilde{\epsilon}$	average strains
η	dimensionless correlation residual
θ	angle
κ	Kolossov's constant
μ	Lamé's modulus
ν	Poisson's ratio
σ_u	standard displacement uncertainty
$\sigma_{\langle u \rangle}$	displacement uncertainty of a given surface
$\sigma_{\bar{\epsilon}}$	standard strain uncertainty
$\sigma_{\tilde{\epsilon}}$	standard strain uncertainty
φ	local correlation residual
$\boldsymbol{\phi}$	reference field of a cracked sample
Φ	global correlation residual
Ω	Analyzed volume
$\langle \bullet \rangle$	mean value of $\bullet$

1 Introduction

Among the different methods available to the engineer or researcher for measuring displacements in a material under mechanical loading, digital image correlation (DIC), whose early developments date back to the early 1980s [1, 2, 3], is gaining growing interest, partly because of the appealing simplicity of the technique, namely, displacement fields are measured by registering two images of the surface of a specimen under different loads [4]. The extension of this technique for measuring three dimensional displacement fields in the *bulk* of samples under load is relatively recent (see for example Ref. [5] for references). Such measurements are complementary to diffraction experiments. First they allow one to relate directly local fluctuations in displacements to variations in the microstructure (in a broad sense) avoiding a combined and usually relatively complex use of diffraction and imaging [6]. Besides, some information can potentially be obtained with correlation methods for amorphous and/or non diffracting materials such as polymeric foams [7] or stone wool [8].

If the principles underlying image and volume correlations are essentially the same, in practice several distinctions must be pointed out. First, 3D images of a material are not as easily obtained in a non destructive way as 2D images. Among the few techniques that provide such 3D images, X-ray tomography using either laboratory or synchrotron X ray sources is more and more used. Tomography images are *reconstructed* from a set of radiographs, a procedure producing artifacts / noise that must be taken into account when digital volume correlation (DVC) measurements are to be performed [9].

Second, as explained before, DVC requires the presence of a pattern in the material microstructure. When observing surfaces, this pattern is easy to obtain by spraying for instance black and white paint [4], in 3D the markers issue is much more complex. Two different methods have been employed so far. A first route is to introduce artificially the markers in the studied material [10, 11, 12, 13, 14], the other one is to directly use the material microstructure [15, 16, 17, 7, 8, 5]. The first method can in principle be applied to a variety

of materials, provided a suitable technique for distributing homogeneously the markers is found. However, the question of how much the presence of those extrinsic features affects the deformation processes remains a critical issue. From that point of view, natural markers appear more attractive, but the number of materials presenting a relevant microstructure is restricted. So far, the deformation of quite different "naturally marked" materials has been studied, namely, trabecular bone [15, 16, 18], polystyrene foam [7], stone wool [8], wood [19], cast iron [20, 5] and aluminum alloys [21, 17] to name a few. It must be pointed out that in some cases [21, 10], the method consists in tracking the displacement of the center of mass of the markers (a method called particle tracking) and is therefore different from what will be described hereafter.

When dealing with 3D images (or volumes), the pattern that is used for measuring displacements fields corresponds to a volume within the material, the term Digital Volume Correlation (DVC) has been chosen and will be used hereafter. Historically, DVC has been first used to characterize relatively large displacement / strain levels such as those obtained during plastic deformation of metallic materials [10] or elastic strains in low moduli materials [15, 7, 8]. The elastic strains in metallic materials being quite small (typically less than 10^{-3}), they are quite challenging to be measured by DVC as the uncertainty levels encountered with this technique tend to be larger than those observed in 2D-DIC [9]. An explanation for these higher uncertainty levels is discussed herein. It is also shown that DVC can be used to evaluate accurately elastic strains in metallic samples under load using synchrotron X ray tomographic images. Finally a variant of DVC, which is called eXtended DVC (or X-DVC [20, 22]), is also described and used for measuring displacement fields in the bulk of a material containing a crack. This technique gives a direct evaluation of crack opening maps and allows for the evaluation of the local crack driving force via the extraction of stress intensity factor profiles [22].

2 Material

The studied material is a ferritic cast iron (3.65 wt%C, 3.2 wt%Si, 0.04 wt%Mg, $<$ 0.1 wt%Mn, $<$0.005 wt%S, 0.02 wt%P) whose microstructure consists of a ferritic matrix containing a homogeneous distribution of nearly spherical graphite nodules (volume fraction: 13 %, average inter-nodule spacing: 50 μm, average nodule diameter: 50 μm). Those nodules have a lower X ray attenuation than the (ferritic) iron matrix, and are therefore easily imaged by tomography; they allow for an easy registration of the reconstructed images. Figure 1(a) shows a reconstructed 3D image of the material in which the nodules appear dark and the ferritic matrix in light colors. The corresponding histogram is shown in Figure 1(b).

[Figure 1 about here.]

3 3D imaging and mechanical tests

The synchrotron tomography experiments were performed at the European Synchrotron Radiation Facility (ESRF) in Grenoble (France) on beamline ID19. The details of the tomography experimental set up of ID19 can be found in Ref. [23]. A set of 600 radiographs (scan) was recorded during a 180-degree rotation on a Charge Coupled Device (CCD) camera with a square array of 2048×2048 pixels (exposure time: 3 s). This detector was coupled with a fluorescent screen via optical lenses. The white beam coming from the synchrotron ring was rendered monochromatic by a multilayered monochromator. The energy of the beam was set to 60 keV. The monochromatic beam was parallel so that no geometric magnification was possible. Instead, the voxel size was the result of the camera optics used.

Reconstruction of the tomographic data was performed with a filtered back-projection algorithm developed at ESRF that provided 8-bit gray scale 3D images with an isotropic voxel size. The nodule size is large enough to allow for a relatively low voxel size to be used for tomography. This, in turn, enables for

the observation of millimetric samples, the only limitation for the sample size being the overall attenuation of the material that has to allow for at least 10 % transmission of the incoming X ray beam. In practice a voxel size of 5.1 μm was chosen so that each finite element in the DVC analysis (see below) could contain at least one nodule (the mean distance between nodules is of the order of 50 μm, or 10 voxels). Therefore analyses dealing with elements whose size is greater than 9 voxels does not need any regularization. For smaller lengths, it is possible to perform successfully a registration (even at the voxel level). This procedure, called voxel-scale DVC (or V-DVC), calls for a mechanical regularization [24].

The first experiment described in this paper consists of a tensile test on a smooth sample (*i.e.,* with no crack) that was loaded to a maximum level of 273 N, and then unloaded. Its cross section is equal to 1.6×0.8 mm^2. Five tomographic scans were acquired during which the load level was equal to 22, 150, 200, 250 and 273 N. The standard uncertainty of the load cell is equal to 5 N. In the second experiment, a specimen containing a crack has been studied during an in situ cyclic test thanks to a dedicated testing machine. This millimetric sample (cross section: 1.6×1.6 mm^2) has been cut out of a larger fatigue coupon [25]. The fatigue machine was directly installed on the rotation stage of the micro-tomography setup. The sample has been cycled in air with a constant stress amplitude (load ratio: $R = 0.1$) and a frequency of 40 Hz. At the beginning of the experiment, scans were acquired at intermediate loading steps from the maximum to the minimum load of the first unloading / loading cycle (Figure 2). Then during the in situ fatigue experiment, scans were recorded at different time intervals with the specimen held under maximum load. When crack growth was detected in these images, another complete loading / unloading sequence was recorded. The fatigue crack interactions with the microstructure gives a roughness of the crack path of the order of the grain/nodule size, which is small enough to ease further modeling. In the present case, one result will be shown when 45,000 cycles were applied to the sample. The reference configuration corresponds to the acquisition at minimum load, and the deformed

configuration to a scan at maximum load.

[Figure 2 about here.]

4 Digital Volume Correlation (DVC)

Volume correlation consists in registering two volumes with the help of a displacement field (to be determined). To estimate the unknown displacement field $\mathbf{u}$, the quadratic difference $\varphi^2 = [f(\mathbf{x}) - g(\mathbf{x} + \mathbf{u}(\mathbf{x}))]^2$ is integrated over the studied domain Ω

$$\Phi^2 = \int_\Omega \varphi^2(\mathbf{x}) \mathrm{d}\mathbf{x} \tag{1}$$

and minimized with respect to the degrees of freedom u_i of the sought displacement field

$$\mathbf{u}(\mathbf{x}) = \sum_j u_j \mathbf{n}_j(\mathbf{x}) \tag{2}$$

where $\mathbf{n}_j(\mathbf{x})$ are the components of the chosen kinematic basis. In the present case, a 3D finite element kinematics is chosen [26] for the sought fields, so that $\mathbf{n}_j$ correspond to shape functions, here selected as trilinear polynomials associated with 8-node cube elements (or C8-DVC [7]). The method used herein is therefore a Galerkin approach to digital volume correlation. Other approaches can be found, namely, as in 2D applications, the most commonly used correlation algorithms consist in registering *locally* small zones of interest in a sequence of pictures to determine local displacement components [4]. The same type of hypotheses are made in three-dimensional algorithms [15, 27, 16, 11]. With C8-DVC there is only one correlation parameter to be chosen, namely, the size ℓ of the element edge.

The second kinematic basis that will be used herein is enriched as in X-FEM simulations [28]. The partition of unity property [29] of the shape functions n_e is used

$$\sum_e n_e(\mathbf{x}) = 1 \tag{3}$$

to construct the enriched approximation of each component u of the displacement field

$$u(\mathbf{x}) = \sum_{j \in \mathcal{N}} u_j n_j(\mathbf{x}) + \sum_{j \in \mathcal{N}_{\text{cut}}} d_j h_j(\mathbf{x}) n_j(\mathbf{x}) \tag{4}$$

where u_j are the degrees of freedom associated with the standard (*i.e.,* continuous) shape functions, and $\mathcal{N}_{\text{cut}}$ the set of nodes that hold additional degrees of freedom d_j associated with the enrichment function $h_j(\mathbf{x})$ defined in [30]

$$h_j(\mathbf{x}) = \mathcal{H}(\mathbf{x}) - \mathcal{H}(\mathbf{x}_j) \tag{5}$$

where $\mathcal{H}$ is the Heaviside step function whose value is 0 below the crack surface and 1 above, and $\mathbf{x}_j$ gives the position of node j. When associated with a C8 shape functions, it is referred to as XC8-DVC [20, 22].

To evaluate the quality of the following correlation results, the normalized correlation residual is considered

$$\eta(\mathbf{x}) = \frac{|\varphi(\mathbf{x})|}{\max_\Omega(f) - \min_\Omega(f)} \tag{6}$$

and its mean value $\langle \eta \rangle$ is computed over the whole correlation volume Ω. When the measured displacements are unknown, this quantity is the only estimator available to assess the quality of the registration (Section 5.1), and the adequacy of the kinematic basis to the analyzed experiment (Section 5.2).

It is to be stressed that the quality of the enriched kinematics relies on the ability to determine precisely the support of the discontinuity, *i.e.,* the crack surface. To reach this goal, it revealed convenient to exploit the residual map obtained with a continuous kinematics [22]. In that case, mismatch errors accumulate on the surface of discontinuity as it violates the kinematic assumption (*i.e.,* continuity of the displacement field). An automatic procedure can then be designed to find a surface which maximizes its intersection with the residual field, thereby providing a good approximation of the crack surface in the reference image.

5 Results and analyses

5.1 Tensile test on smooth sample

To illustrate the usefulness of the correlation residuals, Figure 3 shows the latter ones at different steps of the registration procedure when the first load level is analyzed. In Figure 3(a) the initial difference $|f - g|$ is given before the correlation procedure has started. The microstructure is clearly visible, and $\langle\eta\rangle = 11.6\,\%$. A first step consists in evaluating the mean rigid body translation. The result of this first correction is shown in Figure 3(b). The mean correlation residual $\langle\eta\rangle = 5.4\ \%$ is significantly reduced. However, there are zones for which the registration has still to be improved. Figure 3(c) shows the final difference $|f-g|$ at convergence. The microstructure cannot be recognized, and $\langle\eta\rangle = 2.9\,\%$. This low value gives confidence in the measured displacement field. It is confirmed when the histogram of the gray level residuals (Figure 3(d)) is compared with that of the reference volume (Figure 1(b)).

[Figure 3 about here.]

To evaluate the performance of the correlation code, a reference volume is considered. A constant sub-voxel displacement is applied to create an artificial volume that is registered with the reference one. The mean value is very close to the prescribed one (*i.e.,* a difference less than one thousandth of one voxel). However, there exists a scatter characterized by a standard deviation $\sigma_u = 0.044$ voxel (for 16-voxel elements) whose level is more than one order of magnitude higher than the bias. The value of σ_u is not as low as what is observed in 2D-DIC [31], but classical in DVC. Higher values are generally observed in DVC due to reconstruction artifacts associated with tomography [32, 33, 9].

An additional cause is related to the fact that the analyzed 16-Mvoxel volume is such that its external surface to volume ratio is of the order of $\approx 1/39$ voxel^{-1} as compared with a ratio of external perimeter to surface ratio generally less than $\approx 1/256$ pixel^{-1} for 1-Mpixel pictures. Therefore, the weight of the degrees of freedom belonging to the external faces is more important in the present case

than for regular pictures. Remembering that the degrees of freedom belonging to an external surface have a higher uncertainty level (half of the elements are missing for a node belonging to a face, 3/4 for an edge and 7/8 for a corner), higher surface to volume ratios will lead to higher values of uncertainty levels [24].

Figure 4 illustrates this effect, namely, when only inner nodes are considered (inner ROI), the uncertainty levels are less than when all nodes are considered. The larger the element, the smaller the volume / surface ratio in terms of degrees of freedom. For instance for 8-voxel elements, there are 81% inner nodes. This value falls down to 14% for 64-voxel elements when a $144 \times 288 \times 400$-voxel ROI is considered. This property explains the reason for the difference in terms of measurement uncertainty when only inner nodes are considered or all nodes of the ROI. Figure 4 shows that the larger the element, the smaller the uncertainty. This result is typical of the compromise between measurement uncertainty and spatial resolution. A power law between the displacement uncertainty σ_u and the element size ℓ

$$\sigma_u = \frac{a^{\alpha+1}}{\ell^{\alpha}} \tag{7}$$

where a is a constant expressed in voxels, interpolates very well the results of the uncertainty analysis. The power α is equal to 1.8 when only inner nodes are considered, and 1.1 for all measured nodes. Parameter a is of the order of one voxel in both cases. In the following analyses, 16-voxel C8 elements are used (*i.e.*, $\ell = 16$ voxels).

[Figure 4 about here.]

The raw information provided by DVC is displacement fields. Figure 5 shows 3D renderings of displacement fields in the three directions. It is observed that the main contribution is given by rigid body motions (translation and rotation). However, the latter ones do not reveal the mechanical properties of the material. A post-processing of the displacement field is generally required to study, say, cracked samples [5, 25, 22] or strain fields [7, 8, 18]. Local strains computed from

the gradient of the measured displacement show a large level of fluctuations that may be filtered or smoothed at the expense of faithfulness to the measurement. Global (mean) strains, at the level of the ROI itself, may provide an estimate of, say, the elastic moduli. Mean strains can however be computed in different ways leading to more or less secure determinations.

[Figure 5 about here.]

A first way of evaluating a mean longitudinal strain is to compute the mean displacements of the upper $\langle u_u \rangle$ and lower $\langle u_l \rangle$ faces of the ROI. Let n_x, n_y and n_z denote the number of elements in the x, y, and z directions, respectively. The mean longitudinal strain is defined as

$$\bar{\epsilon}_l = \frac{\langle u_u \rangle - \langle u_l \rangle}{n_z \ell} \tag{8}$$

In the present case, $n_x = 9$, $n_y = 18$, and $n_z = 25$. The total number of measured degrees of freedom is therefore equal to $3(n_x+1)(n_y+1)(n_z+1) = 14,820$. In the following uncertainty analysis, it is assumed that each measured degree of freedom is uncorrelated with any other one. This is only a first approximation. Exact results can be found in Ref. [24]. The standard uncertainty $\sigma_{\langle u \rangle}$ of $\langle u_u \rangle$ and $\langle u_l \rangle$ is therefore equal to

$$\sigma_{\langle u \rangle} = \frac{\sigma_u}{\sqrt{(n_x+1)(n_y+1)}} \tag{9}$$

so that the corresponding standard uncertainty $\sigma_{\bar{\epsilon}}$ of the mean longitudinal strain $\bar{\epsilon}_l$ reads

$$\sigma_{\bar{\epsilon}} = \frac{\sqrt{2}\sigma_u}{\ell n_z \sqrt{(n_x+1)(n_y+1)}} \tag{10}$$

In the present case, $\sigma_{\langle u \rangle} = 0.003$ voxel, and $\sigma_{\bar{\epsilon}} = 1.1 \cdot 10^{-5}$. Figure 6 shows the stress / strain curve deduced from the analysis of the five scans. The identified value of Young's modulus is $E = 187$ GPa.

[Figure 6 about here.]

A second way of evaluating the mean strain is to use all measured points. The corresponding displacement field is linearly interpolated and its first order

gradient is then used to estimate the nominal strain tensor [8]. For the mean longitudinal strain $\hat{\epsilon}$, its standard uncertainty becomes

$$\sigma_{\hat{\epsilon}} = \frac{\sigma_u}{\ell\sqrt{(n_x+1)(n_y+1)\frac{n_z}{6}\left(\frac{n_z}{2}+1\right)(n_z+1)}} \tag{11}$$

so that the two standard strain uncertainties are related by

$$\sigma_{\hat{\epsilon}} = \sigma_{\overline{\epsilon}}\sqrt{\frac{3n_z}{\left(\frac{n_z}{2}+1\right)(n_z+1)}} \tag{12}$$

Equation (12) shows that for values of n_z greater than 2, $\sigma_{\hat{\epsilon}}$ is less than $\sigma_{\overline{\epsilon}}$. When $n_z \gg 1$, the ratio of the two uncertainties is $\sqrt{6/n_z}$. If the level of uncertainty is an issue, it is more desirable to use the interpolation of the whole measured field. However, it has to be checked that the residuals are sufficiently low to make sure that the interpolation is meaningful. In the present case, $\sigma_{\hat{\epsilon}} = 5 \cdot 10^{-6}$. Figure 6 shows the stress / strain curve deduced from the analysis of the five scans. The identified value of Young's modulus is $E = 156$ GPa. This result is in good agreement with classical values of nodular cast iron (160 ± 3 GPa [34, 9]).

5.2 Fatigue test on pre-cracked sample

Figure 7 shows a 3D rendering of the three components of the displacement field of the cracked sample under load obtained by X-FEM after 45,000 fatigue cycles when measured displacements (using X-DVC) are *prescribed* as boundary conditions on the top and bottom faces of the mesh.

[Figure 7 about here.]

As expected, the main opening regime of the crack is in mode I, while some lower amplitude displacements are also recorded in mode II and III. The enriched degrees of freedom in the X-DVC approximation are used to extract 2D maps of the crack opening displacement (COD) for the three modes across the cracked surface at maximum load in Figure 8. It is worth noting that the whole surface was not enriched but only the cracked part. For mode I, the COD changes with the applied load can be found in Ref. [25]. The details of the COD fields are to

be interpreted with caution as measurement uncertainties tend to be larger over the enriched degrees of freedom of the chosen kinematics (see maps of mode II and III CODs of Figure 8). With this point in mind, it can be concluded that the crack is mostly open in mode I and that the enrichment was chosen on a sufficiently large area. Moreover, an approximate determination of the crack geometry (supporting the enrichment) may also induce spurious bias in the evaluation of the opening. Consequently, a quantitative analysis using the raw COD maps is likely to yield poor results in terms of, say, stress intensity factors.

[Figure 8 about here.]

Another way of interpreting the displacements fields measured in the bulk of the specimen is to use them to extract the values of Stress Intensity Factors (SIF) along the crack front. First, least squares techniques were implemented by using 2D solutions [35, 36, 37, 38]. An alternative technique to determine SIFs is to resort to interaction integrals [39, 40, 22]. It was utilized to analyze the results presented in Ref. [22], but will not be used in the following. Instead, the technique proposed by Hamam *et al.* [41] will be followed. It is assumed that each of the node layers orthogonal to the mean direction of the crack front (x, y) plane can be treated separately. For each of these planes (nearly orthogonal to the crack front), the 3D displacement field is projected in a least squares sense onto a basis that includes 2D solutions for a cracked solid (mode I and mode II) as well as mode III asymptotic solutions. Following Williams [42], a closed-form solution for the in-plane displacements $\mathbf{v}$ is derived from Kolossov-Muskhelishvili's potentials

$$\mathbf{v}(r,\theta) = \sum_{p_{\min} \leq p \leq p_{\max}} \left[a_p \boldsymbol{\phi}_I^p(r,\theta) + b_p \boldsymbol{\phi}_{II}^p(r,\theta) \right] \tag{13}$$

where a_p and b_p are real numbers. The reference fields for mode I are

$$\boldsymbol{\phi}_I^p(r,\theta) = \frac{r^{p/2}}{2\mu\sqrt{2\pi}} \left[\kappa e^{ip\theta/2} - \frac{p}{2} e^{i(4-p)\theta/2} + (\frac{p}{2} + (-1)^p) e^{-ip\theta/2} \right] \tag{14}$$

and for mode II

$$\boldsymbol{\phi}^p_{II}(r,\theta) = \frac{ir^{p/2}}{2\mu\sqrt{2\pi}}\left[\kappa e^{ip\theta/2} + \frac{p}{2}e^{i(4-p)\theta/2} - (\frac{p}{2} - (-1)^p)e^{-ip\theta/2}\right] \tag{15}$$

where r and θ denote the in-plane coordinates associated with the usual crack tip frame, μ Lamé's shear modulus, and κ a dimensionless elastic (or Kolossov) coefficient related to Poisson's ratio ν equal to $(3-\nu)/(1+\nu)$ for plane stress conditions, or $3-4\nu$ for plane strain conditions (used in the sequel). The factor $\sqrt{2\pi}$ is introduced to match the usual definitions of K_I and K_{II} SIFs [43], which are thus equal respectively to amplitudes a_1 and b_1 associated with fields $\boldsymbol{\phi}^1_I$ and $\boldsymbol{\phi}^1_{II}$.

Let us first note that the status of fields $\boldsymbol{\phi}^p_I$ and $\boldsymbol{\phi}^p_{II}$ is very different for p less than or greater than 1. For $p > 1$, the fields are called subsingular. They have no impact on the crack tip. Conversely, the attached stress fields increase with the distance to the crack tip. Such functions are thus useful to match the vicinity of the crack tip with the remote geometry, or boundary conditions. For $p < 0$, the fields are referred to as supersingular. Traditionally, the supersingular fields are ignored because their asymptotic behavior near the crack tip is non-physical (*i.e.,* diverging energy density). However, for the present purpose, since the crack tip process zone is cut out from the domain of analysis, these solutions are not rejected [41, 44]. However, it makes no sense to extrapolate them inside the process zone. They rather characterize the (vanishing) influence of non-linearities present in the process-zone in the outer elastic domain. Out-of-plane motions w induced by mode III displacements whose canonical field ϕ^p_{III} reads

$$\phi^p_{III}(r,\theta) = r^{p/2}\cos[p(\theta-\pi)/2] \tag{16}$$

allow one to determine K_{III}. In practice, in-plane solutions are considered for p ranging between -3 and 5. The value $p = -1$ captures the effect of a shift of the crack tip position in the plane with respect to the tip of the equivalent elastic crack [44]. By canceling out its contribution, the equivalent crack tip position is estimated. A length scale proportional to the process zone size [41] is obtained when a_{-3} is related to $a_1 = K_I$. As all odd $p < 0$ functions lead to singular

displacements at the crack tip, the displacement data at nodes whose distance to the crack tip or to the crack mouth is less than 20 voxels are not considered in the analysis. The result of such an extraction is illustrated in Figure 9, which also shows for comparison purposes the results of a numerical extended finite element (X-FEM) calculation based on the real geometry of the crack.

[Figure 9 about here.]

From the results of Figures 7 and 8 it appears that the sample mechanical loading does not correspond to a pure mode I opening of the crack, probably because of slight misalignments between the loading stage and the sample. To overcome this problem, the measured displacement fields were prescribed on the top and bottom surfaces of the analyzed volume. This analysis departs from that proposed in Ref. [22] in which a uniform pressure was considered to match the applied load. Further, the procedure detailed above is used to extract stress intensity factors from the X-FEM displacement field whereas the interaction integral was used in Ref. [22]. When this procedure is carried out, a good agreement between the K_I values extracted from DVC results and those resulting from the X-FEM calculation are obtained (Figure 9). A better agreement is obtained in terms of SIF profiles with the present procedure when compared with that proposed in Ref. [22]. The level of fluctuations in terms of stress intensity factors is similar when X-DVC and X-FEM simulations are compared. This result shows that the fluctuations are not caused by measurement uncertainties alone, but also by the approximate determination of the crack geometry that was the same in X-DVC and X-FEM calculations. Another source of fluctuation might be related to the scale at which the analyses were performed and the corresponding material microstructure, which was modeled as a homogeneous and elastic medium.

By comparing crack opening opening displacement maps and the K_I values obtained by DVC, it has been possible to show that the crack opens at a value of K_I close to 6.5 MPa$\sqrt{\text{m}}$. This value, which has been consistently found for other samples investigated with the same procedure [5, 25], is in very good

agreement with the range of values that are given in the literature for nodular cast iron [5]. It was also possible to clearly correlate crack growth (resp. arrest) to crack opening (resp. closure) [25]. These effects are not discussed herein.

6 Conclusion

Digital volume correlation (DVC) was used to measure displacement fields from 3D synchrotron X-ray tomographic images of cast iron specimens under mechanical loading. The uniform distribution of graphite nodules that are easily imaged by tomography provides a natural pattern for performing correlation avoiding to resort to artificial markers, which might have altered the mechanical behavior of the material. Any other material presenting similar microstructural features could in principle be studied by the same technique. In practice, those features should present an attenuation contrast with the surrounding matrix large enough to be imaged by X rays, and their typical size in the reconstructed images should correspond to a few voxels[1].

For the volumes used analyzed with DVC, the ratio of external surface to volume is larger than that of external perimeter to surface of classical pictures used in 2D correlation. This was shown to be responsible for an increase in uncertainty levels obtained with DVC compared to 2D image correlation. However, it was possible to estimate Young's modulus of the studied material by using DVC (*i.e.,* elastic strains of the order of 10^{-3}) with an accuracy that increased when the whole measured field was used instead of the that of external boundaries to estimate mean strains.

In the case of cracked samples, the use of X-DVC enabled for the measurement of displacement fields even close to the crack surface. Those displacement fields were used to extract stress intensity factors (modes I, II and III) along the crack front. The values obtained were found in good agreement with finite el-

[1] In practice the actual size of the features will depend on the voxel size *i.e.,* on the resolution used, which in turn is given by the dimension of the specimen whose projections should fit on the detector used for tomography [45].

ement calculations when the experimentally measured displacements were used as boundary conditions.

7 Acknowledgements

This work was funded by Agence Nationale de la Recherche under the grant ANR-09-BLAN-0009-01 (RUPXCUBE Project).

References

[1] B. D. Lucas and T. Kanade, An Iterative Image Registration Technique with an Application to Stereo Vision, *Proceedings 1981 DARPA Imaging Understanding Workshop* (1981) 121-130.

[2] P. J. Burt, C. Yen and X. Xu, Local correlation measures for motion analysis: a comparative study, *Proceedings IEEE Conf. on Pattern Recognition and Image Processing*, (1982), 269-274.

[3] M. A. Sutton, W. J. Wolters, W. H. Peters, W. F. Ranson and S. R. McNeill, Determination of Displacements Using an Improved Digital Correlation Method, *Im. Vis. Comp.* **1** [3] (1983) 133-139.

[4] M. A. Sutton, J.-J. Orteu and H. Schreier, *Image correlation for shape, motion and deformation measurements: Basic Concepts, Theory and Applications*, (Springer, New York, NY (USA), 2009).

[5] N. Limodin, J. Réthoré, J.-Y. Buffière, A. Gravouil, F. Hild and S. Roux, Crack closure and stress intensity factor measurements in nodular graphite cast iron using 3D correlation of laboratory X ray microtomography images, *Acta Mat.* **57** [14] (2009) 4090-4101.

[6] M. Preuss, P.J. Withers, E. Maire and J.-Y. Buffière, SiC single fibre full-fragmentation during straining in a Ti-6Al-4V matrix studied by synchrotron X-rays, *Acta Mat.* **50** [12] (2002) 3175-3190.

[7] S. Roux, F. Hild, P. Viot and D. Bernard, Three dimensional image correlation from X-Ray computed tomography of solid foam, *Comp. Part A* **39** [8] (2008) 1253-1265.

[8] F. Hild, E. Maire, S. Roux and J.-F. Witz, Three dimensional analysis of a compression test on stone wool, *Acta Mat.* **57** (2009) 3310-3320.

[9] N. Limodin, J. Réthoré, J. Adrien, J.-Y. Buffière, F. Hild and S. Roux, Analysis and artifact correction for volume correlation measurements using tomographic images from a laboratory X-ray source, *Exp. Mech.* in press (2011) [DOI 10.1007/s11340-010-9397-4].

[10] S. F. Nielsen, H. F. Poulsen, F. Beckmann, C. Thorning and J. A. Wert, Measurements of plastic displacement gradient components in three dimensions using marker particles and synchrotron X-ray absorption microtomography, *Acta Mat.* **51** [8] (2003) 2407-2415.

[11] M. Bornert, J.-M. Chaix, P. Doumalin, J.-C. Dupré, T. Fournel, D. Jeulin, E. Maire, M. Moreaud and H. Moulinec, Mesure tridimensionnelle de champs cinématiques par imagerie volumique pour l'analyse des matériaux et des structures, *Inst. Mes. Métrol.* **4** (2004) 43-88.

[12] A. Germaneau, P. Doumalin and J.-C. Dupré, 3D strain field measurement by correlation of volume images using scattered light: Recording of images and choice of marks, *Strain* **43** [3] (2007) 207-218.

[13] A. Germaneau, P. Doumalin and J.-C. Dupré, Comparison between X-ray micro-computed tomography and optical scanning tomography for full 3D strain measurement by digital volume correlation, *NDT & E International* **41** [6] (2008) 407-415.

[14] K. Haldrup, S. F. Nielsen and J. A. Wert, A general methodology for full-field plastic strain measurements using X-ray absorption tomography and internal markers, *Exp. Mech.* **48** [2] (2008) 199-211.

[15] B. K. Bay, T. S. Smith, D. P. Fyhrie and M. Saad, Digital volume correlation: three-dimensional strain mapping using X-ray tomography, *Exp. Mech.* **39** (1999) 217-226.

[16] E. Verhulp, B. van Rietbergen and R. Huiskes, A three-dimensional digital image correlation technique for strain measurements in microstructures, *J. Biomech.* **37** [9] (2004) 1313-1320.

[17] H. Toda, I. Sinclair, J.-Y. Buffière, E. Maire, K. H. Khor, P. Gregson and T. Kobayashi, A 3D measurement procedure for internal local crack driving forces via synchrotron X-ray microtomography, *Acta Mat.* **52** [5] (2004) 1305-1317.

[18] A. Benoit, S. Guérard, B. Gillet, G. Guillot, F. Hild, D. Mitton, J.-N. Périé and S. Roux, 3D analysis from micro-MRI during in situ compression on cancellous bone, *J. Biomech.* **42** (2009) 2381-2386.

[19] F. Forsberg, R. Mooser, M. Arnold, E. Hack and P. Wyss, 3D micro-scale deformations of wood in bending: Synchrotron radiation μCT data analyzed with digital volume correlation, *J. Struct. Biol.* **164** (2008) 255-262.

[20] J. Réthoré, J.-P. Tinnes, S. Roux, J.-Y. Buffière and F. Hild, Extended three-dimensional digital image correlation (X3D-DIC), *C. R. Mécanique* **336** (2008) 643-649.

[21] H. Toda, I. Sinclair, J.-Y. Buffière, E. Maire, T. Connolley, M. Joyce, K. H. Khor and P Gregson, Assessment of the fatigue crack closure phenomenon in damage-tolerant aluminium alloy by in-situ high-resolution synchrotron X-ray microtomography, *Phil. Mag.* **83** [21] (2003) 2429-2448.

[22] J. Rannou, N. Limodin, J. Réthoré, A. Gravouil, W. Ludwig, M.-C. Baietto, J.-Y. Buffière, A. Combescure, F. Hild and S. Roux, Three dimensional experimental and numerical multiscale analysis of a fatigue crack, *Comp. Meth. Appl. Mech. Eng.* **199** (2010) 1307-1325.

[23] W. Ludwig, J.-Y. Buffière, S. Savelli and P. Cloetens, Study of the interaction of a short fatigue crack with grain boundaries in a cast Al alloy using X-ray microtomography, *Acta Mat.* **51** [3] (2003) 585-598.

[24] H. Leclerc, J.-N. Périé, S. Roux and F. Hild, Voxel-scale digital volume correlation, *Exp. Mech.* in press (2011) DOI 10.1007/s11340-010-9407-6.

[25] N. Limodin, J. Réthoré, J.-Y. Buffière, F. Hild, S. Roux, W. Ludwig, J. Rannou and A. Gravouil, Influence of closure on the 3D propagation of fatigue cracks in a nodular cast iron investigated by X-ray tomography and 3D Volume Correlation, *Acta Mat.* **58** [8] (2010) 2957-2967.

[26] O. C. Zienkievicz and R. L. Taylor, *The Finite Element Method*, (McGraw-Hill, London (UK), 4th edition, 1989).

[27] T. S. Smith, B. K. Bay and M. M. Rashid, Digital volume correlation including rotational degrees of freedom during minimization, *Exp. Mech.* **42** [3] (2002) 272-278.

[28] N. Moës, J. Dolbow and T. Belytschko, A finite element method for crack growth without remeshing, *Int. J. Num. Meth. Eng.* **46** [1] (1999) 133-150.

[29] I. Babuska and J. M. Melenk, The partition of unity method, *Int. J. Num. Meth. Eng.* **40** [4] (1997) 727-758.

[30] G. Zi and T. Belytschko, New crack-tip elements for XFEM and applications to cohesive cracks, *Int. J. Num. Meth. Eng.* **57** [15] (2003) 2221-2240.

[31] G. Besnard, F. Hild and S. Roux, "Finite-element" displacement fields analysis from digital images: Application to Portevin-Le Chatelier bands, *Exp. Mech.* **46** (2006) 789-803.

[32] G. R. Davis and J. C. Elliot, Artefacts in X-ray microtomography of materials, *Mat. Sci. Eng.* **22** [9] (2006) 1011-1018.

[33] R. A. Ketcham, New algorithms for ring artefact removal, in: *Developments in X-Ray Tomography V*, U. Bonse, eds., (SPIE, Bellingham Wa, 2006), **6318** 00-1-15.

[34] P. Dierickx, *Etude de la microstructure et des mécanismes d'endommagement de fontes G.S. ductiles : influence des traitements thermiques de ferritisation*, (PhD dissertation, INSA de Lyon, 1996).

[35] S. R. McNeill, W. H. Peters and M. A. Sutton, Estimation of stress intensity factor by digital image correlation, *Eng. Fract. Mech.* **28** [1] (1987) 101-112.

[36] J. Abanto-Bueno and J. Lambros, Investigation of crack growth in functionally graded materials using digital image correlation, *Eng. Fract. Mech.* **69** (2002) 1695-1711.

[37] S. Roux and F. Hild, Stress intensity factor measurements from digital image correlation: post-processing and integrated approaches, *Int. J. Fract.* **140** [1-4] (2006) 141-157.

[38] S. Yoneyama, T. Ogawa and Y. Kobayashi, Evaluating mixed-modestress intensity factors from full-field displacement fieldsobtained by optical methods, *Eng. Fract. Mech.* **74** (2007) 1399-1412.

[39] J. Réthoré, A. Gravouil, F. Morestin and A. Combescure, Estimation of mixed-mode stress intensity factors using digital image correlation and an interaction integral, *Int. J. Fract.* **132** (2005) 65-79.

[40] J. Réthoré, S. Roux and F. Hild, Noise-robust Stress Intensity Factor Determination from Kinematic Field Measurements, *Eng. Fract. Mech.* **75** [13] (2008) 3763-3781.

[41] R. Hamam, F. Hild and S. Roux, Stress intensity factor gauging by digital image correlation: Application in cyclic fatigue, *Strain* **43** (2007) 181-192.

[42] M. L. Williams, On the stress distribution at the base of a stationary crack, *ASME J. Appl. Mech.* **24** (1957) 109-114.

[43] G. R. Irwin, Analysis of the Stresses and Strains near the End of a Crack Traversing a Plate, *ASME J. Appl. Mech.* **24** (1957) 361-364.

[44] S. Roux, J. Réthoré and F. Hild, Digital Image Correlation and Fracture: An Advanced Technique for Estimating Stress Intensity Factors of 2D and 3D Cracks, *J. Phys. D: Appl. Phys.* **42** (2009) 214004.

[45] J.-Y. Buffière, E. Maire, J. Adrien, J.-P. Masse and E. Boller, In Situ Experiments with X ray Tomography: an Attractive Tool for Experimental Mechanics, *Exp. Mech.* **50** [3] (2010) 289-305.

List of Figures

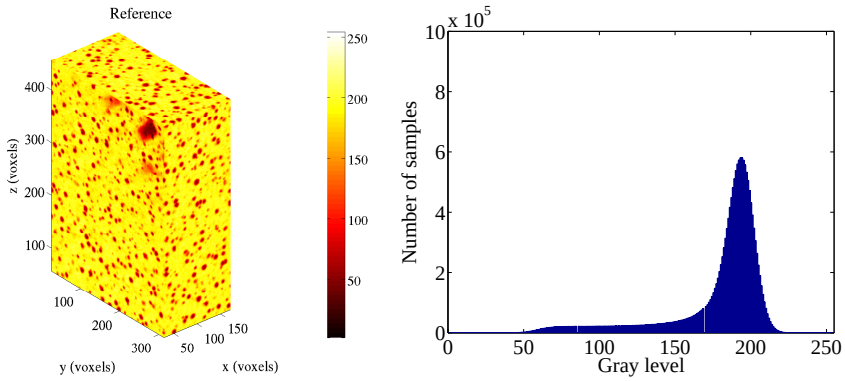

(a) (b)

Figure 1: ROI (a) of the analyzed volume in Section 5.1 ($144 \times 288 \times 400$ voxels, 1 voxel $\leftrightarrow$ 5.1 μm, 8-bit digitization) and corresponding gray level histogram (b).

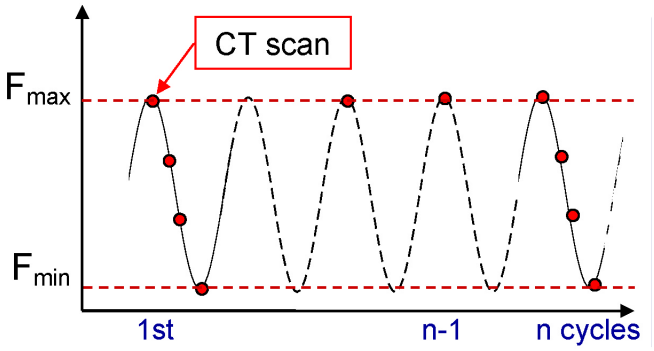

(a)

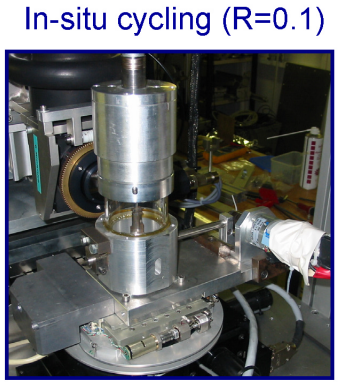

(b)

Figure 2: Schematic illustration of the tests performed (a). A red point corresponds to the acquisition of one tomographic scan. Several scans at different load levels are recorded to perform DVC measurements during the fatigue test. Picture of the in situ testing machine mounted on the tomographic set up (b).

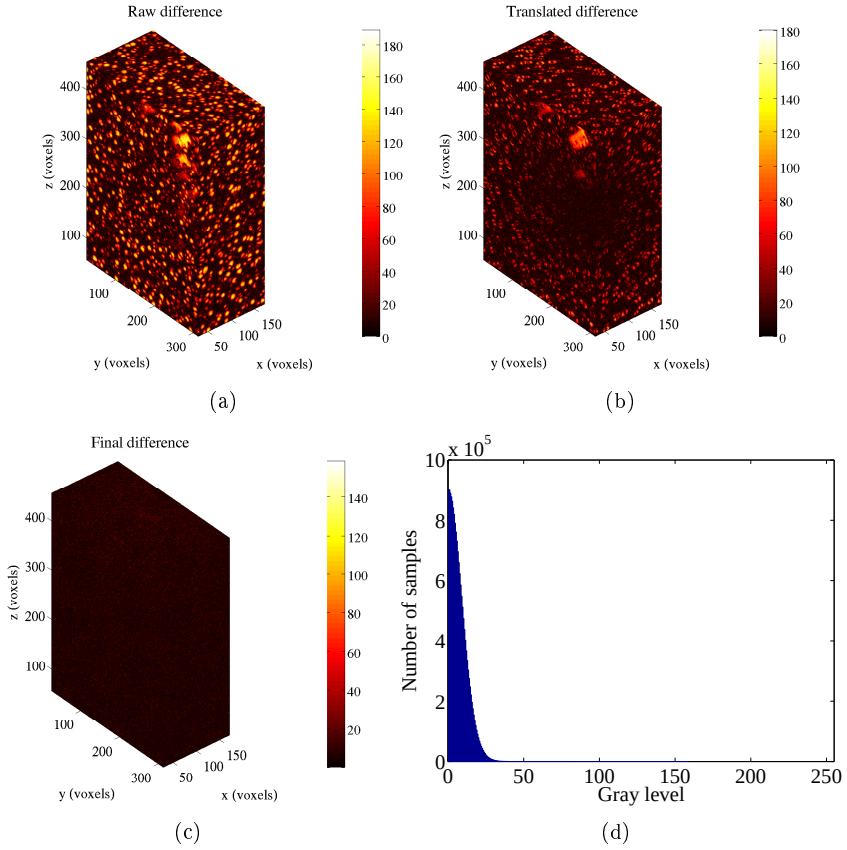

Figure 3: Initial (a), with rigid body translation correction (b), and at convergence (c) gray level residuals $|f - g|$ when the first load level is analyzed. The final histogram of gray level residuals (d) can be compared with that of the reference volume shown in Figure 1(b).

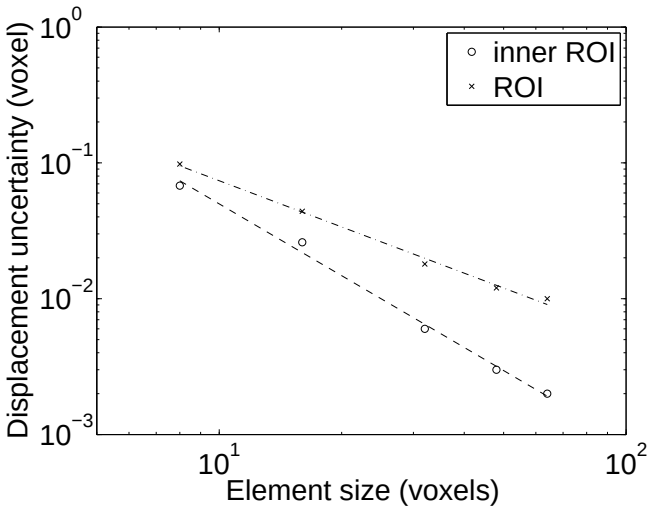

Figure 4: Standard displacement uncertainty σ_u as a function of the element size ℓ for C8-DVC applied to the reference volume shown in Figure 1 when shifted by 0.5 voxel in all three directions. The dashed lines correspond to a power law interpolation [Equation (7)].

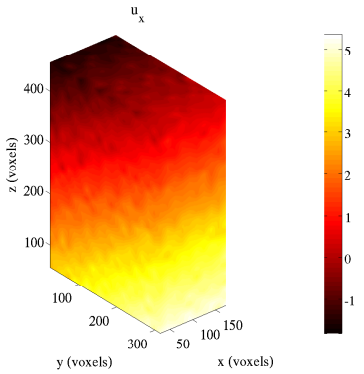

(a)

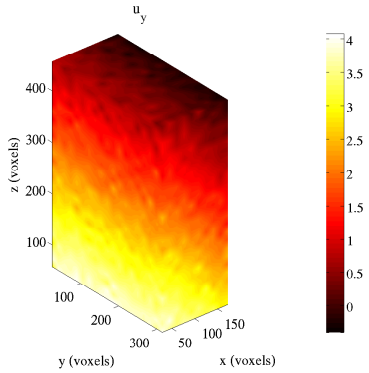

(b)

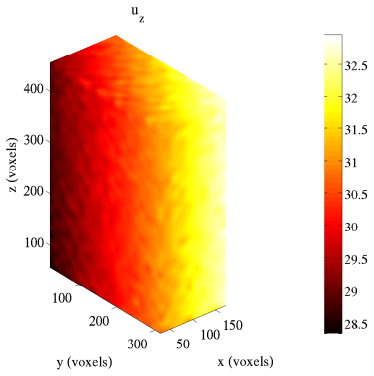

(c)

Figure 5: 3D rendering of transverse (a,b) and longitudinal (c) displacement fields expressed in voxels (1 voxel $\leftrightarrow$ 5.1 μm).

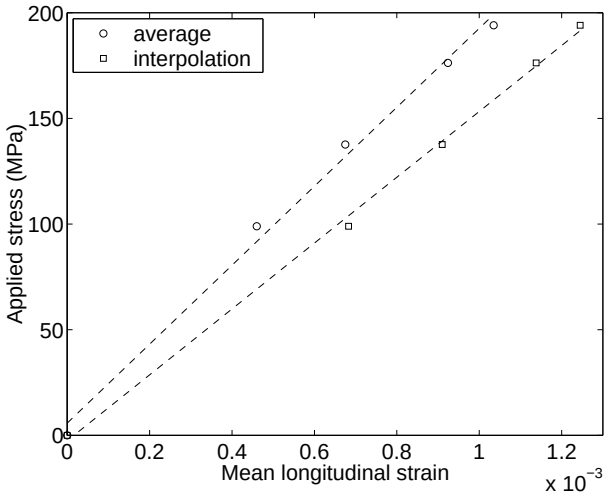

Figure 6: Stress / strain plot for the two ways of evaluating the mean strain. The dashed lines show a linear interpolation used to estimate the macroscopic Young's modulus.

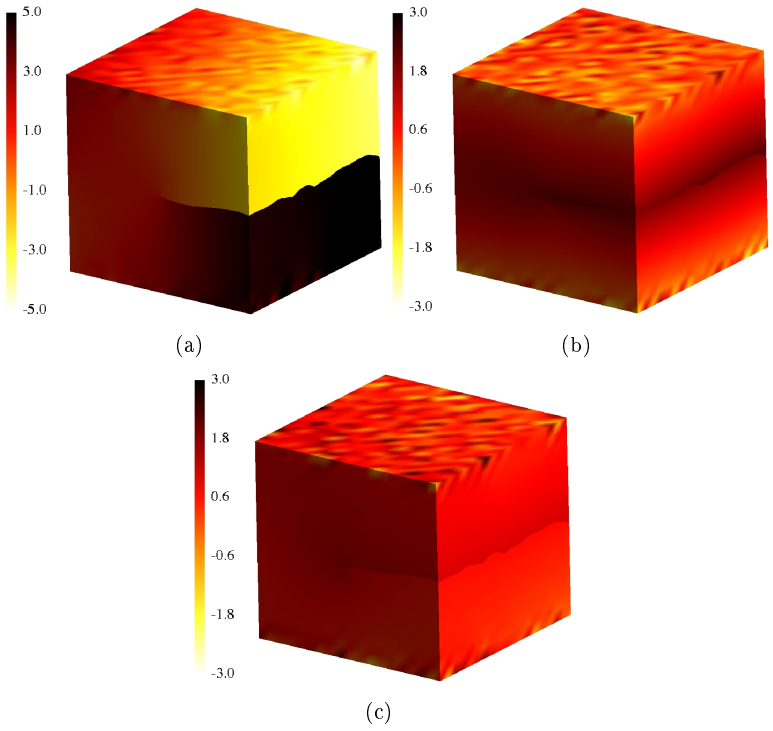

Figure 7: 3D rendering of the displacement fields calculated by X-FEM in the cracked sample under maximum load after 45,000 fatigue cycles: longitudinal (a), in-plane (b), and out-of-plane (c) directions. The scale bar is expressed in micrometers, the cube edge is 288-voxel long (*i.e.*, 1.46 mm). The boundary conditions used for the calculation correspond to the experimental displacements obtained by X-DVC.

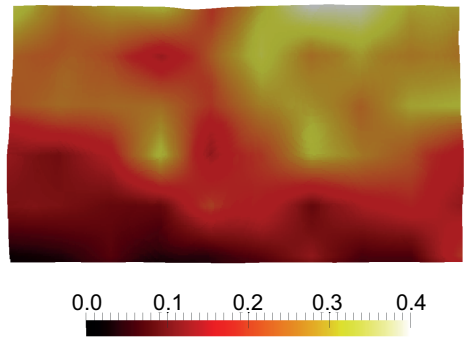

(a)

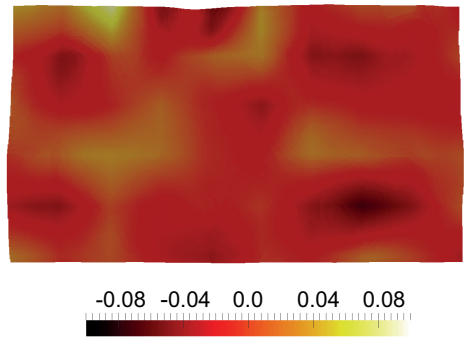

(b)

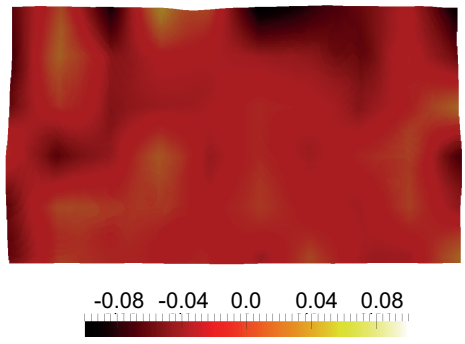

(c)

Figure 8: Maps of crack opening displacement for modes I (a), II (b), and III (c) at maximum load after 45,000 cycles. The displacements are expressed in voxels (1 voxel $\leftrightarrow$ 5.1 μm). The crack front is close to the lower edge.

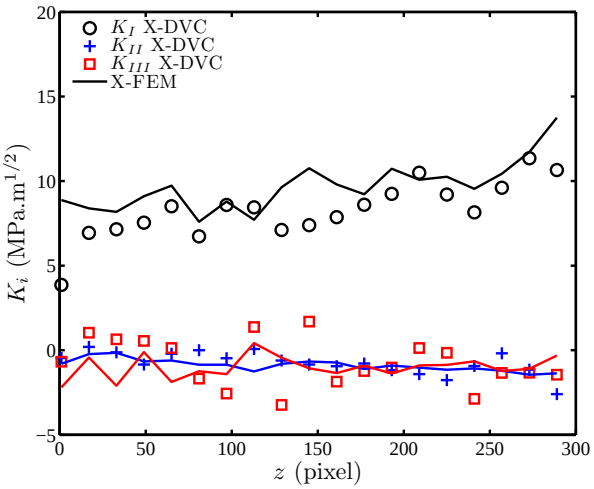

Figure 9: Profiles of K_I, K_{II} and K_{III} along the crack front at the maximum load of the fatigue cycle after 45,000 cycles determined experimentally by post-processing X-DVC results, and numerically by resorting to X-FEM analyses.